J Adv Ceram

Research Article

Synergistically enhances piezoelectricity and resistivity of high-temperature $0.3Na_{0.5}Bi_{2.5}Nb_2O_9$–$0.7Bi_3TiNbO_9$ ceramics by (W,Cr) co-doping

Zhipeng Zhang†, Fusheng Song†, Qilai Wen, Zong-Yang Shen✉, Zhumei Wang, Wenqin Luo

Cite this article: Zhang Z, Song F, Wen Q, et al. *J Adv Ceram* 2026, **15**(5): 9221281. https://doi.org/10.26599/JAC.2026.9221281

ABSTRACT: $0.3Na_{0.5}Bi_{2.5}Nb_2O_9$–$0.7Bi_3Ti_{1-x}(W_{1/3}Cr_{2/3})_xNbO_9$ (0.3NBN–0.7BTN–WC_x, x = 0–0.06) high Curie temperature piezoceramics with a bismuth layered structure were prepared by a solid-state reaction method. The optimized 0.3NBN–0.7BTN–$WC_{0.04}$ ceramics possess an enhanced piezoelectric constant (d_{33} = 20.3 pC/N) with a very high Curie temperature (T_C = 845.9 °C). The incorporation of W/Cr ions disrupts the long-range order of the crystal lattice, which induces significant distortion of the [Nb/Ti]O_6 octahedral and generates more stable domain structures, contributing to an enhanced piezoelectric response and high Curie temperature. Meanwhile, W^{6+} donor doping and the formation of $(Cr'_{Ti} - V_{\ddot{O}})$ defect dipoles synergistically reduced the concentration of oxygen vacancies, thereby achieving both a high resistivity (ρ = 7.3×10^7 Ω·cm) and a low dielectric loss (tanδ = 0.057) under high temperature conditions (@500 °C). In addition, the d_{33} of the 0.3NBN–0.7BTN–$WC_{0.04}$ ceramics exhibits excellent thermal stability, retaining 93.1% of its initial value (d_{33} = 18.9 pC/N) after annealing at 600 °C. All results indicate that 0.3NBN–0.7BTN–$WC_{0.04}$ ceramics can be good candidates for piezoelectric sensor applications in high-temperature harsh environments.

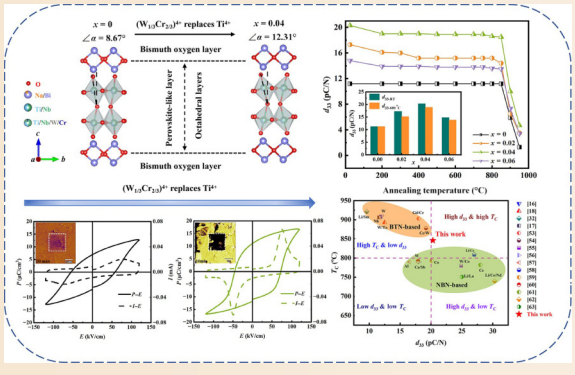

KEYWORDS: bismuth layer-structured ceramics; high-temperature piezoelectrics; $Na_{0.5}Bi_{2.5}Nb_2O_9$; Bi_3TiNbO_9; defect structure

1 Introduction

Piezoelectric materials are functional materials that can realize the efficient conversion between electrical energy and mechanical energy. It is widely used in aerospace, geological exploration, nuclear power, and other fields [1–3]. With the rapid development of the high-tech industry, the performance and working temperature of piezoelectric devices are facing new challenges. For instance, the fabrication of aeroengine vibration monitoring sensors requires piezoelectric ceramic materials with a high Curie temperature (T_C), a reasonable piezoelectric coefficient (d_{33}), and high temperature resistivity. Compared with toxic lead-based ceramics, lead-free piezoelectric ceramics such as $BaTiO_3$ (BT), $Na_{0.5}Bi_{0.5}TiO_3$ (NBT), and $K_{0.5}Na_{0.5}NbO_3$ (KNN) are not only environmentally friendly but also have excellent piezoelectric properties (d_{33} ≥ 400 pC/N). However, their relatively low T_C (normally < 350 °C) makes these materials prone to failure under high-temperature conditions [4–8]. Bismuth layer-structured ferroelectrics (BLSFs) have garnered significant attention due to their high T_C (normally > 500 °C), excellent thermal stability, low aging characteristics, and low dielectric loss tangent (tanδ) [9,10]. The structure of BLSFs consists of alternating perovskite-like blocks $(A_{m-1}B_mO_{3m+1})^{2-}$ and fluorite-like bismuth oxide $(Bi_2O_2)^{2+}$ layers along the *c*-axis. The A-site in the structure accommodates monovalent, divalent, and trivalent ions, while the hexacoordinated B-site is designed for transition metal cations. The typical value range of m is 1–6, representing the number of [BO_6] octahedral layers [11,12].

Bismuth titanate niobate (Bi_3TiNbO_9, BTN) is a typical two-layer BLSF compound composed of perovskite-like $(BiTiNbO_7)^{2-}$ layers sandwiched between bismuth oxide layers $(Bi_2O_2)^{2+}$ along the *c*-axis. BTN ceramics are considered promising high-temperature piezoelectric materials due to their high T_C (~910 °C) and excellent thermal stability [13–15]. Nevertheless, the spatial rotation restriction of polarization, high coercive field (E_C), and low resistivity (ρ) result in a low piezoelectric coefficient (d_{33} ≤ 3 pC/N) of pure BTN ceramics, severely hindering their practical applications in high-temperature electronic devices. In recent

† Zhipeng Zhang and Fusheng Song contributed equally to this work.

Jiangxi Key Laboratory of Advanced Ceramic Materials, China National Light Industry Key Laboratory of Functional Ceramic Materials, School of Materials Science and Engineering, Jingdezhen Ceramic University, Jingdezhen 333403, China.

✉ Corresponding author. E-mail: shenzongyang@163.com

Received: February 3, 2026; Revised: March 2, 2026; Accepted: March 10, 2026

decades, extensive research has demonstrated that chemical doping is considered a simpler and more effective method to improve the piezoelectric properties of BTN ceramics. For example, the introduction of high-valence cations (e.g., Nb^{5+}, Ta^{5+}, and W^{6+}) as donor dopants into the B-site of BTN ceramics can effectively suppress the formation of oxygen vacancies. This, in turn, lowers the electrical conductivity and coercive field, thereby enhancing the piezoelectric properties [16–18]. Meanwhile, it has been reported that A-site Ce^{4+} doping in BTN ceramics can also achieve a relatively high electrical resistivity (1.2×10^6 Ω·cm at 500 °C) and an enhanced piezoelectric coefficient (d_{33} = 17.1 pC/N) [19]. However, current reports suggest that it is very difficult to achieve a d_{33} value exceeding 20 pC/N for BTN-based ceramics with either A-site or B-site doping. On the other hand, $Na_{0.5}Bi_{2.5}Nb_2O_9$ (NBN) ceramics, which are also two-layer BLSF compounds, also have a high T_C of ~790 °C, but their piezoelectric constant is not high ($d_{33} \approx$ 9.2 pC/N) [20]. Based on the typical BLSF compound with m = 2 for both BTN and NBN, we have recently successfully prepared a new xNBN–(1–x)BTN ferroelectric solid solution ceramic, which exhibits improved piezoelectric properties (d_{33} = 11.2 pC/N) and a high T_C of 848.4 °C at the optimized composition x = 0.3 [21]. However, its piezoelectric properties need to be further improved to meet the requirements of high-temperature sensor manufacturing.

The use of a composite cation co-doping strategy has been found to significantly improve the piezoelectric properties of BLSF ceramics, such as W/Cr-modified $Bi_4Ti_3O_{12}$ ceramics and Ce/Ta co-doped $Bi_3Ti_{1.5}W_{0.5}O_9$ ceramics [22,23]. Based on this consideration, in this work, a B-site $(W_{1/3}Cr_{2/3})^{4+}$ complex ion doping strategy was adopted to further optimize the composition, achieving both an enhanced piezoelectric constant (d_{33} = 20.3 pC/N) and high resistivity (7.3×10^7 Ω·cm at 500 °C). By analyzing the intrinsic lattice distortion and domain structure, the mechanism of electrical property improvement was systematically investigated and explained. This work provides a new method for the preparation of BLSF ceramics that balance high T_C and high piezoelectric properties for high-temperature sensor applications.

2 Experimental

Sample synthesis: $0.3Na_{0.5}Bi_{2.5}Nb_2O_9$–$0.7Bi_3Ti_{1-x}(W_{1/3}Cr_{2/3})_xNbO_9$ (abbreviated as 0.3NBN–0.7BTN–WC_x, x = 0, 0.02, 0.04, and 0.06) ceramics were prepared by a solid-state reaction method using Na_2CO_3 (99.8%), Bi_2O_3 (99.9%), TiO_2 (99.9%), WO_3 (99.9%), Cr_2O_3 (99.9%), and Nb_2O_5 (99.0%) (Sinopharm Chemical Reagent Co., Ltd., China) as raw materials. The raw materials were weighed and mixed by ball-milling in ethanol for 24 h according to their nominal composition. The mixed slurries were dried and calcined in air at 800 °C for 3 h. Afterward, the calcined powders were ball-milled for 24 h and then dried again. After granulation using polyvinyl alcohol solution (PVA, 5 wt%), the powders were pressed into green pellets with a diameter of 12 mm and a thickness of approximately 1 mm under a pressure of 10 MPa. The green pellets were sintered at temperatures ranging from 1020 to 1080 °C for 2 h after eliminating the PVA binders at 650 °C for 3 h. Finally, the sintered samples were polished, coated with silver paste, and fired at 650 °C for 40 min to form electrodes.

Structural characterization: The phase purity and crystal structure of the ceramics were identified using an X-ray diffractometer (XRD; D8-Advance, Bruker, Germany) with Cu Kα radiation in the 2θ range of 20°–70°, with a step of 0.02° and a counting time of 1.2 s per step. Rietveld refinement of the XRD data was performed using GSAS-II software. The surface morphology of the ceramics was observed using a field-emission scanning electron microscope (FE-SEM; JSM-5610LV, Japan). Room-temperature Raman spectra were obtained by a Raman scattering spectrometer (in Via, Renishaw, UK), where the spectral excitation was provided by a 532 nm laser. The oxygen vacancy concentration was evaluated by an X-ray photoelectron spectrometer (XPS; Escalab 250XI, Thermo Scientific, USA). The domain structure of the polished samples was observed using a piezoelectric force microscope (PFM; MFP-3D, Asylum Research, USA), which was characterized utilizing polished and unpolarized ceramics by applying a voltage of 30 V in a scanning area of 5 μm × 5 μm.

Electrical property measurements: The dielectric properties as a function of temperature were measured at 100 kHz using a precision impedance analyzer (TH2828S, Changzhou Tonghui Electronic Co., Ltd., China). The direct current (DC) resistivity from 200 to 600 °C (at 25 °C intervals) was determined using an insulation resistance tester (TH2684, Changzhou Tonghui Electronic Co., Ltd., China) connected to a programmable mini-furnace. The polarization–electric field (P–E) and current–electric field (I–E) hysteresis loops were characterized at 160 °C and 10 Hz using a ferroelectric system (Trek model 609B, Radiant, USA). The impedance data were analyzed with an impedance analyzer (Agilent 4294 A, Agilent Technologies Inc.). For piezoelectric measurements, the samples were poled in silicone oil at 160 °C under a DC electric field of 100–130 kV/cm for 20–30 min. The piezoelectric coefficient (d_{33}) was then measured at room temperature using a quasi-static d_{33} meter (ZJ-3A, Institute of Acoustics, Chinese Academy of Sciences, China). To evaluate thermal stability, the poled samples were annealed at different temperatures for 1 h, followed by d_{33} measurements at room temperature after each annealing step.

3 Results and discussion

Figure 1(a) shows the room temperature XRD patterns of 0.3NBN–0.7BTN–WC_x ceramics in the 2θ range of 20°–70°. Obviously, the diffraction peaks observed in all the samples exhibit a good match with the standard diffraction card (PDF#039-0233). The strongest peak corresponds to the (115) plane, which aligns with the characteristic that the highest intensity reflection for BLSF ceramics with m = 2 occurs on the $(11\underline{2}\ m+1)$ plane [17,24]. Moreover, no secondary phase is detected upon W/Cr incorporation, confirming the successful diffusion of W^{6+} and Cr^{3+} into the 0.3NBN–0.7BTN lattice. As shown in Fig. 1(b), the $(20\underline{1}0)/(02\underline{1}0)$ peaks gradually split from an initial single peak to double peaks at $x \geq 0.02$, indicating a change in crystal symmetry and an increase in orthogonality. However, with a further increase in x to 0.06, the intensity of these peaks weakens, suggesting a reduction in orthogonal distortion. Figure 1(c) provides a schematic of the Bi_3TiNbO_9 crystal structure, featuring alternating $(Bi_2O_2)^{2+}$ layers and perovskite-type blocks. To quantitatively assess the structural evolution, Rietveld refinement of XRD data was performed using GSAS-II software. The refined lattice parameters a, b, and c are presented in Fig. 1(d), and it can be seen that the parameters b and c decrease for $x \leq 0.04$. This phenomenon can be attributed to the higher electronegativity of W/Cr (W: 2.36, Cr: 1.66) compared with Ti (1.54) and Nb (1.6), leading to shortened Ti/Nb–O bonds in octahedra and a reduction in cell volume (V). When $x \geq 0.04$, the parameters b and c increase, which is related to the ionic radius of complex $(W_{1/3}Cr_{2/3})^{4+}$ (r_i = 0.61 Å, coordination number (CN) = 6) being larger than that of Ti (r_i = 0.605 Å, CN = 6), thus inducing lattice expansion. In contrast, parameter a shows an inverse trend. The degree of orthorhombic distortion was assessed using the a/b

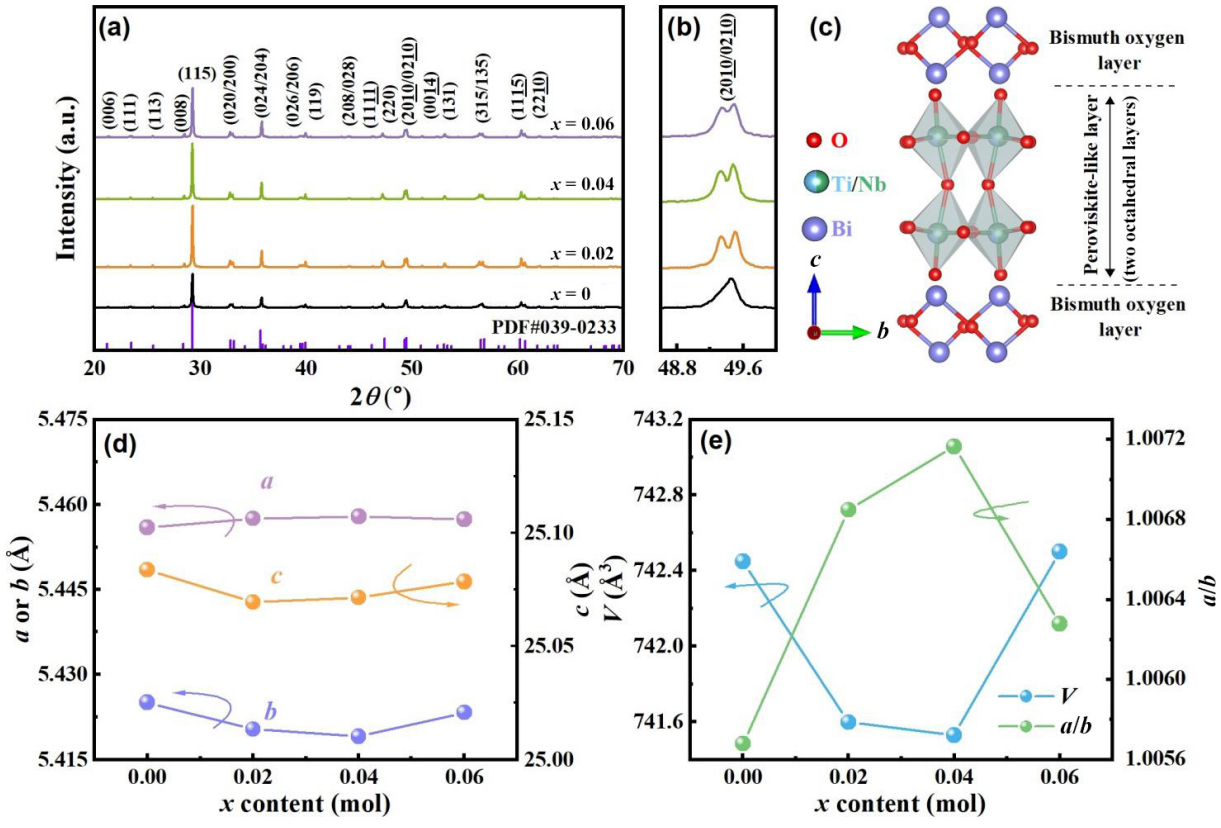

Fig. 1 (a) Room temperature XRD patterns of 0.3NBN–0.7BTN–WC_x ceramics and (b) local magnification diagram. (c) Schematic crystal structure of BTN ceramics. (d) Refined lattice parameters as a function of x. (e) Unit-cell volume and orthorhombic distortion a/b versus x.

ratio, where higher values indicate greater structural distortion [25,26]. As depicted in Fig. 1(e), the a/b ratio first increases from 1.0057 (x = 0) to a maximum of 1.0071 (x = 0.04) and then decreases to 1.0062 (x = 0.06), highlighting that the maximum lattice distortion occurs at x = 0.04.

Figures 2(a) and 2(b) show the Rietveld-refined XRD patterns for the ceramics with x = 0 and x = 0.04, respectively. As seen, each fitted curve aligns closely with the original data, with reliability factors (R_{wp}) remaining below 7% and goodness of fit (GOF) values below 2 for both samples. These results indicate a high degree of confidence in the refinement outcomes. To further visualize the impact of W/Cr co-doping on the crystal structure of 0.3NBN–0.7BTN ceramics, structural visualization was conducted using Vesta software based on the refined data, as depicted in Fig. 2(c). The angle α(s$\angle O_2$–O_1-c), which reflects the octahedral tilt relative to the c-axis, increases from 8.67° to 12.31° with W/Cr co-doping. The maximum α values occur at x = 0.04, consistent with the highest degree of lattice distortion indicated by the a/b ratio in Fig. 1(e). Such structural modifications play a key role in enhancing the piezoelectric performance of ceramics [27,28].

Figure 3(a) shows the Raman spectra of 0.3NBN–0.7BTN–WC_x ceramics in the wavenumber range of 50–1000 cm^{-1}. All samples exhibit similar spectral features, confirming the formation of a single orthorhombic phase regardless of the W/Cr co-doping level. For the representative composition x = 0.04, the spectrum can be well fitted using Lorentzian profiles, as displayed in Fig. 3(b), and is decomposed into twelve distinct Raman modes (v1–v12) [19]. The Raman spectra for all samples in Fig. 3(a) can be divided into three characteristic regions. In the low-wavenumber region (0–200 cm^{-1}), the modes correspond to the vibrations of Bi^{3+} in the $(Bi_2O_2)^{2+}$ layers and the A-site vibrations in the perovskite-like layers [29,30]. As shown in Fig. 3(c), the positions of modes v1–v3 in this region (0–200 cm^{-1}) show no significant shift with doping, indicating that W/Cr co-doping has little influence on the $(Bi_2O_2)^{2+}$ layers and A-site ions. In the intermediate wavenumber region (200–400 cm^{-1}), the v5 mode, assigned to the bending vibrations of O–(Ti/Nb)–O bonds within the octahedra, shifts to higher wavenumbers and then decreases, reaching a maximum at x = 0.04. This behavior reflects the maximum distortion of the oxygen octahedra at this composition [27,31]. Moreover, in the high-wavenumber region (≥ 400 cm^{-1}), a significant Raman shift to lower wavenumbers can be observed for the v8 and v9 modes, which may be related to the reverse shift of the oxygen atoms in the oxygen octahedron, thus leading to a change in the structure of the oxygen octahedron. In contrast, the v12 mode, corresponding to the symmetric stretching of the $[Nb/Ti]O_6$ octahedra, shifts to higher wavenumbers as the lighter Ti^{4+} ions are replaced by the heavier $(W_{1/3}Cr_{2/3})^{4+}$ complex ions [32,33]. Additionally, the peaks of v8 and v9 gradually broaden, and their intensities decrease with increasing doping content, as observed in Fig. 3(a). These changes suggest that the introduction of $(W_{1/3}Cr_{2/3})^{4+}$ enhances the local structural disorder, which is beneficial for improving the dielectric properties of the ceramics.

Figures 4(a)–4(d) show the SEM images of the 0.3NBN–0.7BTN–WC_x ceramics. All samples are nearly fully dense with well-bonded grains. Furthermore, the microstructures exhibit a typical anisotropic sheet-like grain morphology, which originates from faster grain growth along the a–b plane than along the c-axis for BLSF ceramics [34,35]. The average grain size, estimated using the Nano Measurer software, ranges from 2.11 to 2.66 μm, as shown in the inset of Figs. 4(a)–4(d). Upon the addition of $(W_{1/3}Cr_{2/3})^{4+}$ complex ions, Fig. 4(b) reveals the presence of some abnormally large grains, indicating that appropriate $(W_{1/3}Cr_{2/3})^{4+}$ complex ions can promote grain growth behavior. This phenomenon may be related to the formation of a liquid phase

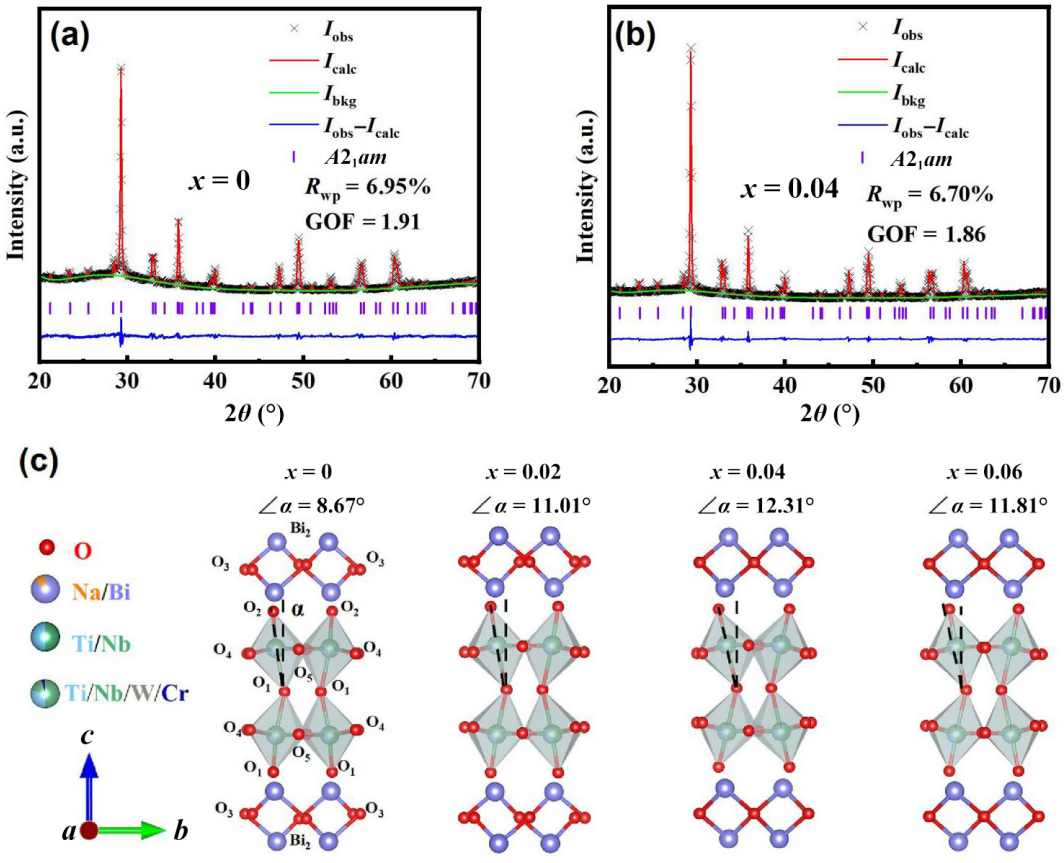

Fig. 2 (a, b) Rietveld refinement for 0.3NBN–0.7BTN–WC_x ceramics (x = 0, 0.04). (c) Visualization of crystal structures and octahedral tilting for each component.

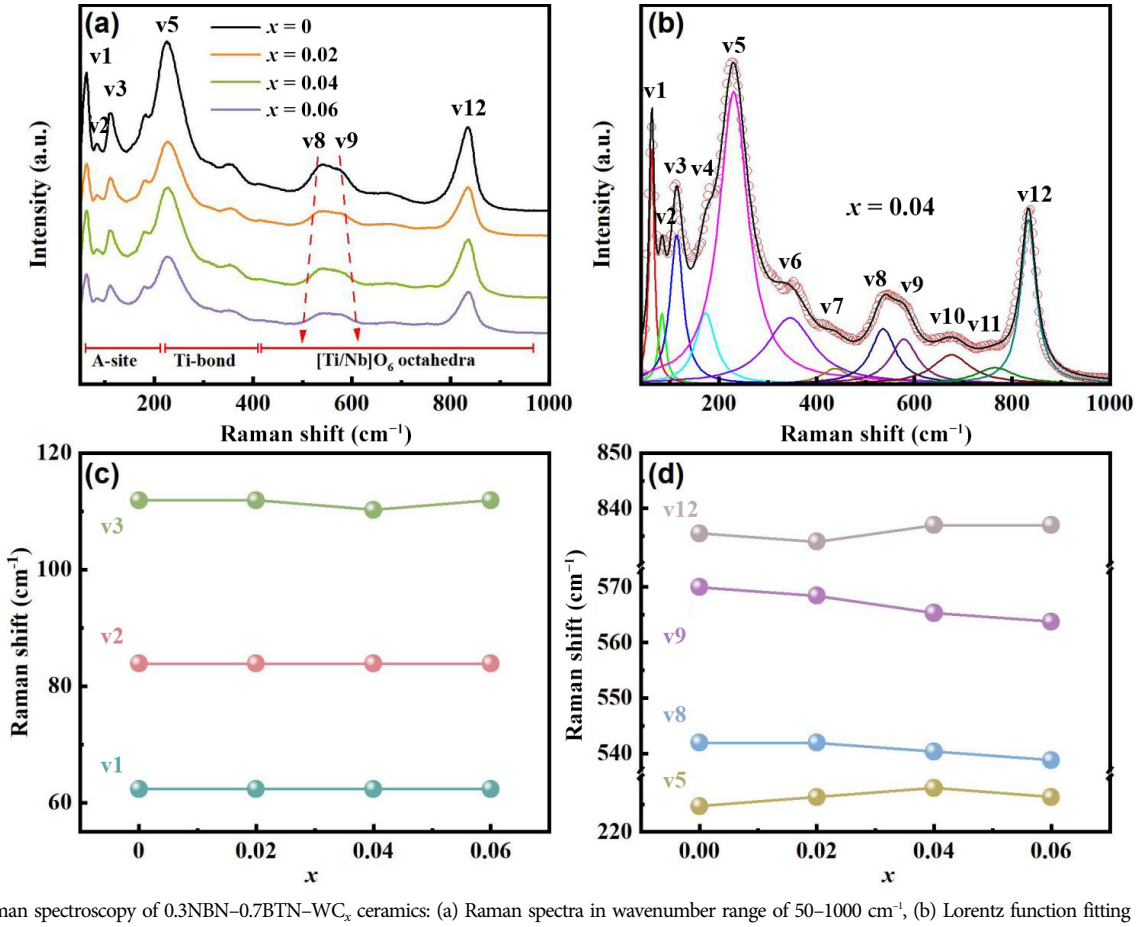

Fig. 3 Raman spectroscopy of 0.3NBN–0.7BTN–WC_x ceramics: (a) Raman spectra in wavenumber range of 50–1000 cm^{-1}, (b) Lorentz function fitting of x = 0.04 ceramics, and (c, d) variation of v1, v2, v3, v5, v8, v9, and v12 as a function of x value.

induced by the volatilization of Bi and the fluxing effect of Cr_2O_3, and a nonuniform distribution of this liquid phase would favor localized abnormal grain growth. However, with further increases in the $(W_{1/3}Cr_{2/3})^{4+}$ complex ion content (Figs. 4 (c) and 4(d)), the number of abnormally large grains decreases. This reduction can be attributed to mutual impingement of growing grains as the amount of liquid phase increases, thereby restricting further abnormal growth. Similar grain growth behavior has also been reported in our previous work on BIT-based BLSF ceramics [36].

Figure 5(a) presents the temperature-dependent dielectric permittivity (ε_r) and dielectric loss (tanδ) for 0.3NBN–0.7BTN–WC_x ceramics measured at 100 kHz. All samples display a single dielectric peak in their response curves, indicating a phase transition from the polar ferroelectric phase to the paraelectric phase in BLSFs, corresponding to the Curie temperature T_C [37]. Figure 5(b) shows the T_C values for all samples. The T_C value decreases monotonically with increasing W/Cr co-doping content. As is widely recognized, dielectric loss is a critical parameter for evaluating the performance of piezoelectric ceramics. Figure 5(c) displays the dielectric loss at 500 °C ($\tan\delta_{500°C}$) and the relative dielectric loss ($\tan\delta_{500°C}/\tan\delta_{RT}$, where $\tan\delta_{RT}$ denotes the dielectric loss at room temperature). As illustrated in Fig. 5(c), the

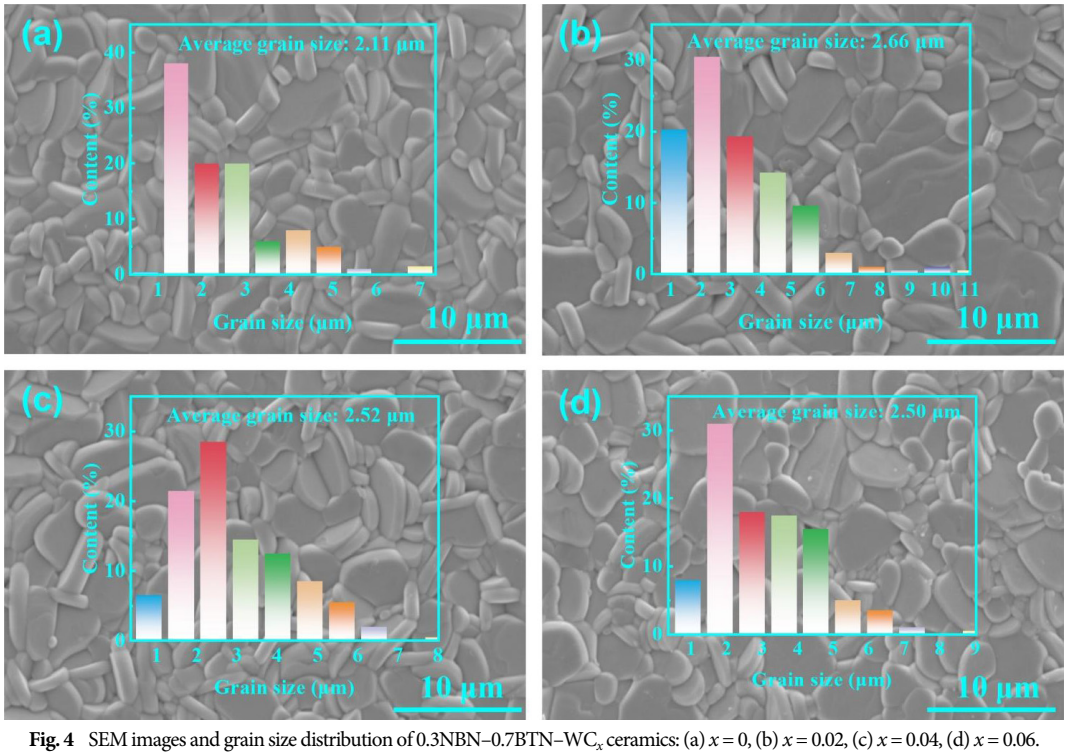

Fig. 4 SEM images and grain size distribution of 0.3NBN–0.7BTN–WC_x ceramics: (a) $x = 0$, (b) $x = 0.02$, (c) $x = 0.04$, (d) $x = 0.06$.

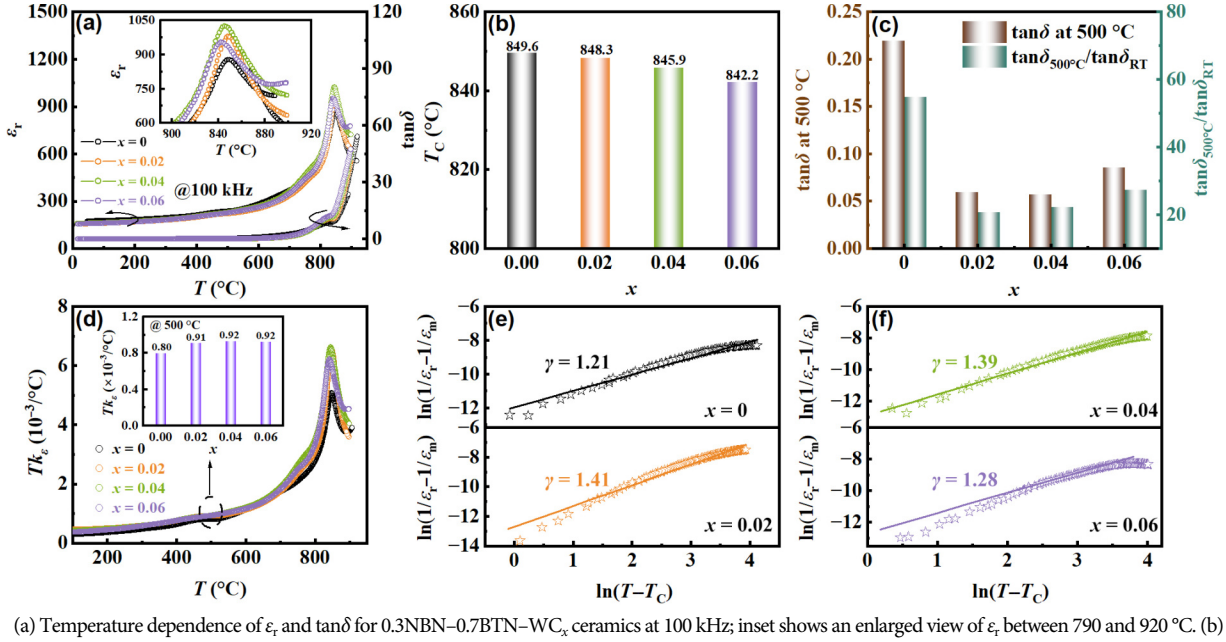

Fig. 5 (a) Temperature dependence of ε_r and tanδ for 0.3NBN–0.7BTN–WC_x ceramics at 100 kHz; inset shows an enlarged view of ε_r between 790 and 920 °C. (b) T_C as a function of W/Cr doping content. (c) $\tan\delta_{500°C}$ and $\tan\delta_{500°C}/\tan\delta_{RT}$ as a function of W/Cr doping content. (d) Tk_ε as a function of temperature; inset presents Tk_ε at 500 °C for all compositions. (e, f) Plots of $\ln(1/\varepsilon_r - 1/\varepsilon_m)$ versus $\ln(T - T_C)$ at 100 kHz for 0.3NBN–0.7BTN–WC_x ceramics.

清華大学出版社 Tsinghua University Press | SciOpen

introduction of W/Cr results in a significant reduction in both $\tan\delta_{500°C}$ and $\tan\delta_{500°C}/\tan\delta_{RT}$. This decrease can be attributed to a lower concentration of internal carriers, and this conclusion was later confirmed by XPS. To assess the dielectric stability of the samples, the temperature coefficient of the dielectric constant was calculated using Eq. (1):

$$Tk_\varepsilon = \frac{\varepsilon_T - \varepsilon_{T_0}}{\varepsilon_{T_0}(T - T_0)} \quad (1)$$

where ε_{T_0} and ε_T represent the dielectric constant at room temperature (T_0) and at temperature T, respectively [27,38]. The variation in Tk_ε with temperature is shown in Fig. 5(d). The inset indicates that the dielectric stability remains nearly unchanged up to 500 °C. For the x = 0.04 sample at 500 °C, Tk_ε is as low as 0.92×10^{-3}/°C, demonstrating excellent dielectric temperature stability.

To further investigate the effect of W/Cr co-doping on the relaxor properties of 0.3NBN–0.7BTN ceramics, the modified Curie–Weiss equation was employed, as given by Eq. (2):

$$\frac{1}{\varepsilon_r} - \frac{1}{\varepsilon_m} = C^{-1}(T - T_m)^\gamma \quad (2)$$

where C is a constant; T_m is the temperature corresponding to the maximum dielectric constant ε_m; γ represents the degree of dispersion [39]. The plots of $\ln(1/\varepsilon_r - 1/\varepsilon_m)$ versus $\ln(T - T_C)$ at 100 kHz are given in Figs. 5(e) and 5(f). It can be observed that the γ value increases from 1.21 (x = 0) to 1.39 (x = 0.04), suggesting that W/Cr co-doping enhances the diffuseness of the ceramics, thereby improving their dielectric relaxation properties. This phenomenon is attributed to the increased disorder of B-site ions, which is consistent with the Raman analysis results shown in Fig. 3. This relaxation structure can disrupt long-range ordered ferroelectric domains, leading to a decrease in domain wall energy. Under the action of an electric field, domains are more easily flipped, thereby enhancing the piezoelectric properties of ceramics [40].

Figure 6(a) shows the resistivity of 0.3NBN–0.7BTN–WC_x ceramics as a function of temperature. The DC resistivity of all samples decreases with increasing temperature, indicating that the conductive carriers in these ceramics are thermally activated [41]. At high temperature (≥ 500 °C), the resistivity of samples with moderate W/Cr co-doping is higher than that of undoped 0.3NBN–0.7BTN ceramics. This phenomenon can be attributed to two factors: First, the introduction of W/Cr reduces the oxygen vacancy concentration in ceramics, and second, the 0.3NBN–0.7BTN–WC_x ceramics exhibit a dense microstructure and a low dielectric loss. Figure 6(b) displays the temperature-dependent conductivity of 0.3NBN–0.7BTN–WC_x ceramics. The conductivity profiles can be divided into two regions: a low-temperature region (≤ 350 °C) and a high-temperature region (≥ 350 °C). In the low-temperature range, the conductivity varies noticeably with composition, whereas above 350 °C, the compositional dependence becomes much weaker, suggesting different conduction mechanisms in the two regions. Therefore, the activation energy (E_a) for DC resistivity was calculated using the Arrhenius equation: $\rho = A\exp(E_a/kT)$, where A is the

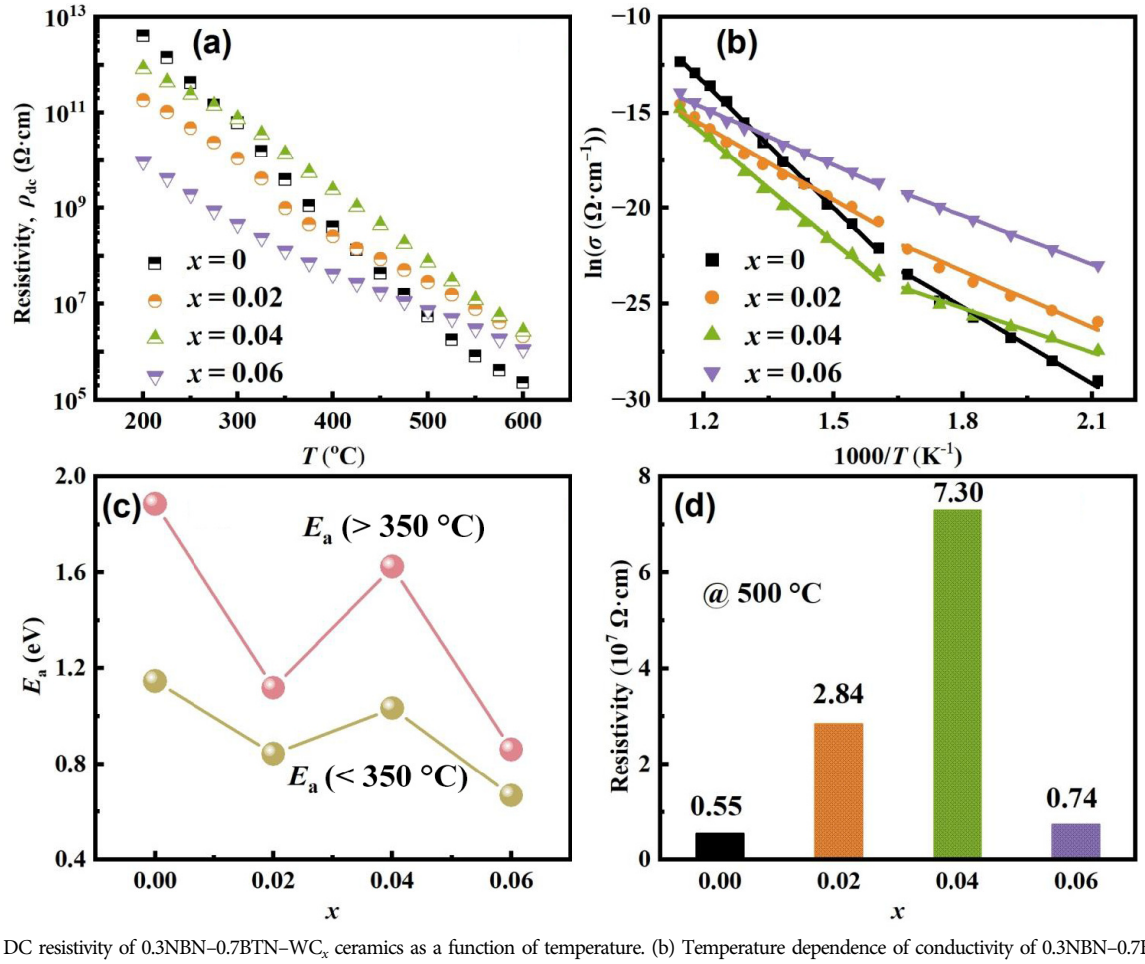

Fig. 6 (a) DC resistivity of 0.3NBN–0.7BTN–WC_x ceramics as a function of temperature. (b) Temperature dependence of conductivity of 0.3NBN–0.7BTN–WC_x ceramics. (c) Activation energy (E_a) of all ceramics as a function of x at low and high temperatures. (d) DC resistivity of ceramics at 500 °C.

preexponential, E_a the activation energy of the charge carrier, k the Boltzmann constant, and T the Kelvin temperature [42]. Furthermore, the calculated E_a values for all samples are shown in Fig. 6(c). In the low-temperature region, E_a lies between 0.6 and 1.15 eV, which closely corresponds to the second ionization activation energy of oxygen vacancies (0.6–1.2 eV) [43]. This indicates that the conductivity mechanism at lower temperatures is mainly dominated by defects and impurities. Such defects originate mainly from Bi_2O_3 volatilization during the sintering process (Reaction (3)). According to the charge compensation principle, the introduced W^{6+} substitutes for Ti^{4+} at the B-site, and the extra electrons compensate for the hole contribution (Reactions (4)–(6)). Meanwhile, the lower-valence Cr^{3+} cation doping promotes the formation of a strong combined defect dipole $\left(Cr'_{Ti} - V^{\cdot\cdot}_{O}\right)$ in the 0.3NBN–0.7BTN–WC_x ceramics (Reaction (7)). As a result, oxygen vacancies are confined around the defect centers and do not participate in the conduction process. In the high-temperature region, E_a ranges from 0.82 to 1.89 eV, approximately half of the band-gap energy ($E_g \approx 3.4$ eV). This implies that the conductivity of the doped ceramics at elevated temperature is primarily attributed to intrinsic thermally activated ionic conduction [44]. Figure 6(d) presents the resistivity of all samples at 500 °C. Notably, the 0.3NBN–0.7BTN–$WC_{0.04}$ sample maintains a high resistivity of 7.3×10^7 Ω·cm at this temperature, indicating its ability to withstand higher applied poling electric fields. This contributes to enhanced polarization efficiency and improved piezoelectric constant d_{33}.

$$Bi_2O_3 \rightarrow Bi_2O_3(gas)\uparrow + 2V'''_{Bi} + 3V^{\cdot\cdot}_{O} \quad (3)$$

$$W^{6+} \xrightarrow{Ti^{4+}} W^{\cdot\cdot}_{Ti} + 2e' \quad (4)$$

$$V^{\cdot\cdot}_{O} + \frac{1}{2}O_2 \rightarrow O^{\times}_{O} + 2h^{\cdot} \quad (5)$$

$$e' + h^{\cdot} \rightarrow \text{null} \quad (6)$$

$$Cr_2O_3 \xrightarrow{Ti^{4+}} 2Cr'_{Ti} + V^{\cdot\cdot}_{O} + 3O^{\times}_{O} \quad (7)$$

Figures 7(a) and 7(b) present the $-Z'$–Z'' complex impedance plots for the $x = 0$ and $x = 0.04$ samples over a temperature range from 480 to 600 °C and a frequency range from 100 Hz to 1 MHz. The impedance data were fitted using the equivalent circuit model (R/C/CPE) in Z-View software, where R, C, and CPE represent the resistance, capacitance, and constant phase element, respectively. The semicircular arcs derived from the fitting process show excellent agreement with the experimental data. Notably, the radii of the Nyquist plot semicircles decrease as the temperature increases, indicating negative temperature coefficients of resistance. Furthermore, the centers of all Nyquist plot semicircles lie below the Z' axis, consistent with Maxwell–Wagner (M–W) relaxation behavior [45]. Additionally, for both the $x = 0$ and $x = 0.04$ samples, the impedance data exhibit single semicircles within the temperature range of 480–600 °C, indicating that the electrical conduction in this range is primarily governed by the grain interior, with negligible contributions from grain boundaries or electrode interfaces. The impedance of the W/Cr co-doped sample ($x = 0.04$) is an order of magnitude higher than that of the undoped ceramic ($x = 0$). The E_a of 0.3NBN–0.7BTN–$WC_{0.04}$ grains was calculated to be 1.31 eV using the Arrhenius equation, indicating an increase in activation energy and a reduction in oxygen vacancy defects compared with the pure 0.3NBN–0.7BTN sample ($x = 0$, $E_a = 1.02$ eV). These results demonstrate that W/Cr co-doping effectively suppresses the oxygen vacancy concentration and improves the high-temperature performance. Figures 7(c) and 7(d) show the frequency dependence of impedance imaginary components for 0.3NBN–0.7BTN–WC_x ($x = 0$, 0.04) ceramics across the frequency range from 100 Hz to 1 MHz at various temperatures. The gradual shift of relaxation peaks to higher frequencies with increasing temperature suggests thermally activated relaxation processes. Figures 7(e) and 7(f) present the normalized Z''/Z''_{max} and M''/M''_{max} as functions of frequency at 480 °C. The non-overlapping peaks indicate that short-range carrier migration dominates the relaxation mechanism, while long-range migration predominates below f_{max}

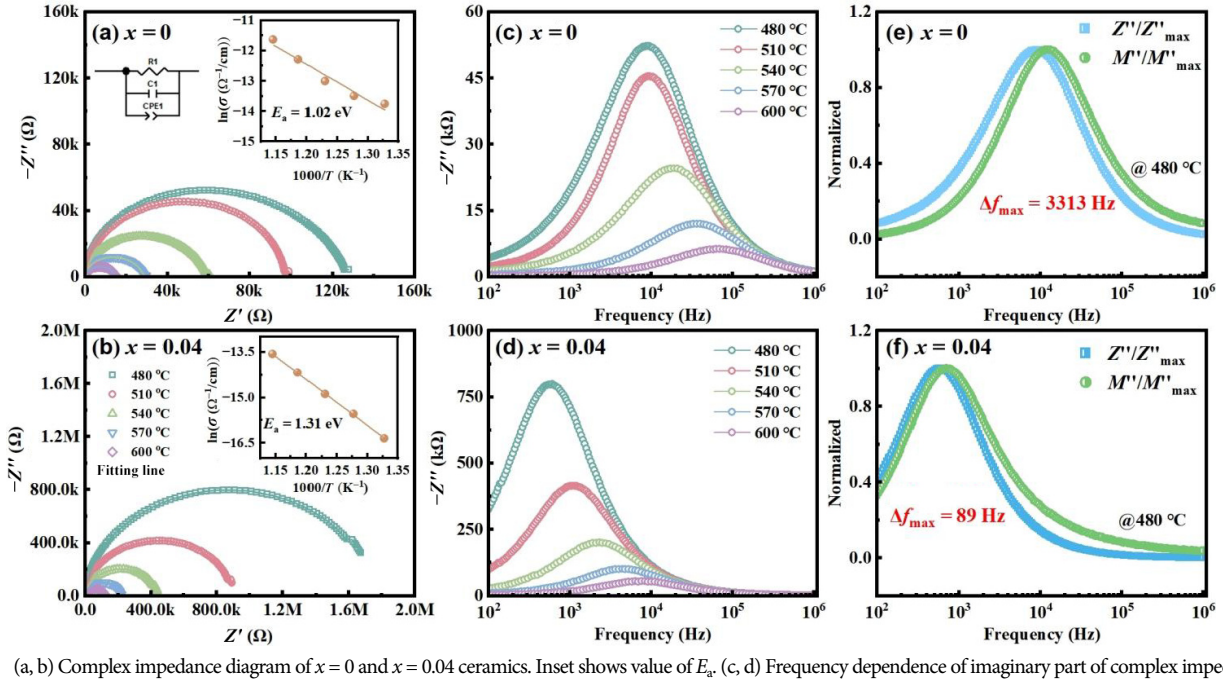

Fig. 7 (a, b) Complex impedance diagram of $x = 0$ and $x = 0.04$ ceramics. Inset shows value of E_a. (c, d) Frequency dependence of imaginary part of complex impedance for $x = 0$ and $x = 0.04$ ceramics at different temperatures. (e, f) Normalized Z''/Z''_{max} and M''/M''_{max} versus frequency at 480 °C for $x = 0$ and $x = 0.04$.

[46]. Furthermore, the x = 0.04 sample exhibits significantly lower f_{max} and Δf_{max} values than the undoped ceramic, highlighting that W/Cr co-doping effectively suppresses long-range carrier migration and charge inhomogeneity, thereby enhancing the overall electrical properties [47].

To examine the variation in oxygen vacancy concentration, XPS data were analyzed and fitted using Advantage software. The survey spectrum of the 0.3NBN–0.7BTN–WC_x ceramics is shown in Fig. 8(a), and the corresponding elements are determined. High-resolution O 1s and Bi 4f spectra for the compositions x = 0 and x = 0.04 are displayed in Figs. 8(b) and 8(c). The O 1s spectrum was deconvoluted into three distinct peaks: lattice oxygen (O_{latt}) at 529.7 eV, oxygen vacancy (O_V) at 531.4 eV, and adsorbed oxygen (O_{ads}) at 532.3 eV. The ratio of O_{vac}/O_{latt} is typically used to estimate the oxygen vacancy concentration in ceramics [46,48]. Area ratio analysis revealed that increasing the W/Cr doping level x to 0.04 reduced this ratio from 0.75 to 0.54, indicating that appropriate W/Cr co-doping effectively suppresses the formation of oxygen vacancies. Furthermore, Bi $4f_{7/2}$ and Bi $4f_{5/2}$ binding energy peaks were observed at 158.9 and 164.2 eV, respectively. Notably, the Bi^{3+} binding energy peaks remained unchanged after doping, confirming the stable valence state of Bi in the samples.

Figures 9(a)–9(d) show the P–E hysteresis loops and the corresponding I–E curves for 0.3NBN–0.7BTN–WC_x ceramics measured at 160 °C and 10 Hz. Compared with the undoped ceramic (x = 0), W/Cr co-doping clearly enhances the saturation of the P–E loops. Specifically, the x = 0.04 sample exhibits fully saturated P–E loops and significantly higher current peaks. This indicates that W/Cr disrupts the long-range ordered structures of the ferroelectric, promoting the formation of smaller domains with lower energy barriers, thereby improving the polarization response of the ceramic under an applied electric field. However, further increasing the doping level to x = 0.06, the P–E loops become flatter and wider, and the I–E curves are weakened. This can be attributed to an increased defect concentration caused by excessive doping, which impedes the domain response to the polarizing electric field, resulting in a decline in ferroelectric performance. Moreover, W/Cr co-doping induces asymmetry in the P–E loops ($E_C^+ \neq E_C^-$), which is ascribed to the generation of defect dipoles $\left(Cr_{Ti}^{'}\text{-}V_{O}^{\cdot\cdot}\right)$ that participate in the polarization process, leading to the creation of a bias field within the ceramic. However, this asymmetric phenomenon is largely suppressed at x = 0.06, indicating that excessive W/Cr co-doping causes the redistribution of defect carriers, which partially shields polarized charges and macroscopically manifests as attenuation of the built-in electric field and piezoelectric performance. To further investigate the influence of W/Cr co-doping on the ferroelectric properties of 0.3NBN–0.7BTN ceramics. Figures 9(e) and 9(f)

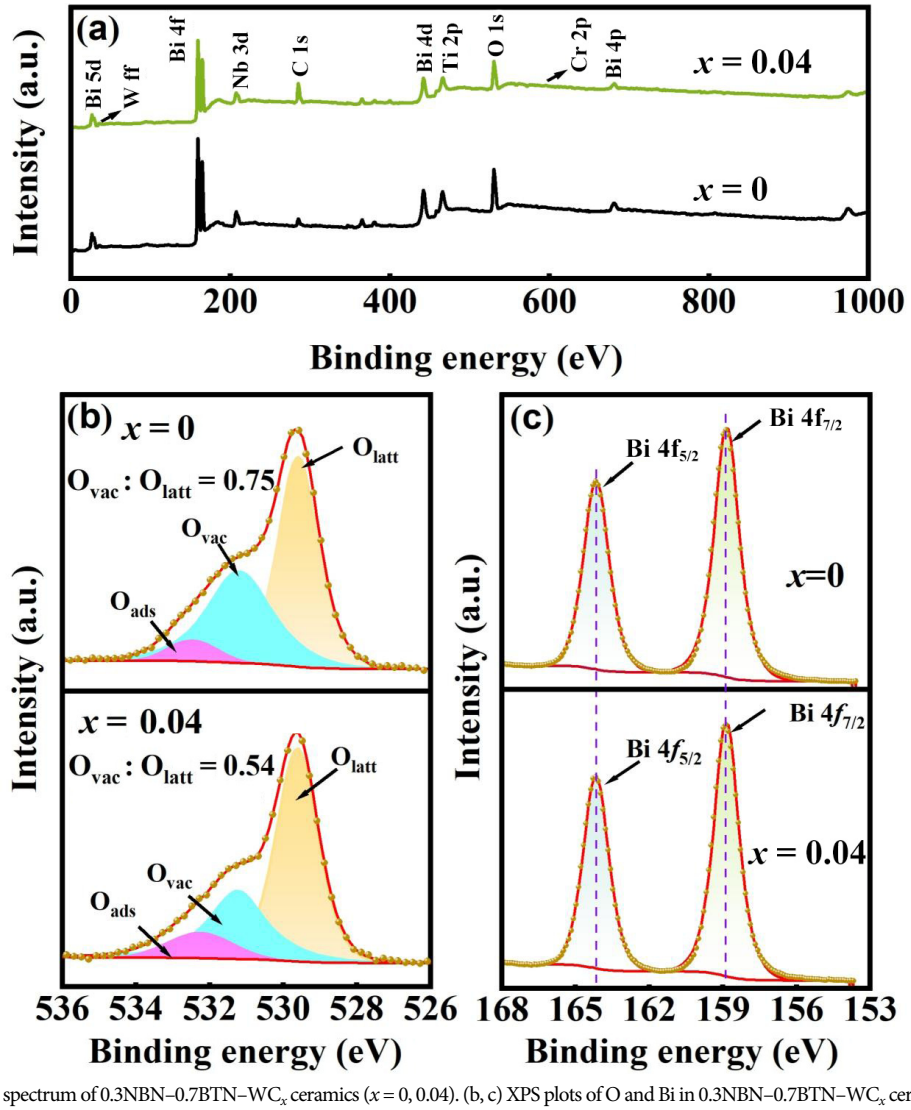

Fig. 8 (a) XPS full spectrum of 0.3NBN–0.7BTN–WC_x ceramics (x = 0, 0.04). (b, c) XPS plots of O and Bi in 0.3NBN–0.7BTN–WC_x ceramics (x = 0, 0.04).

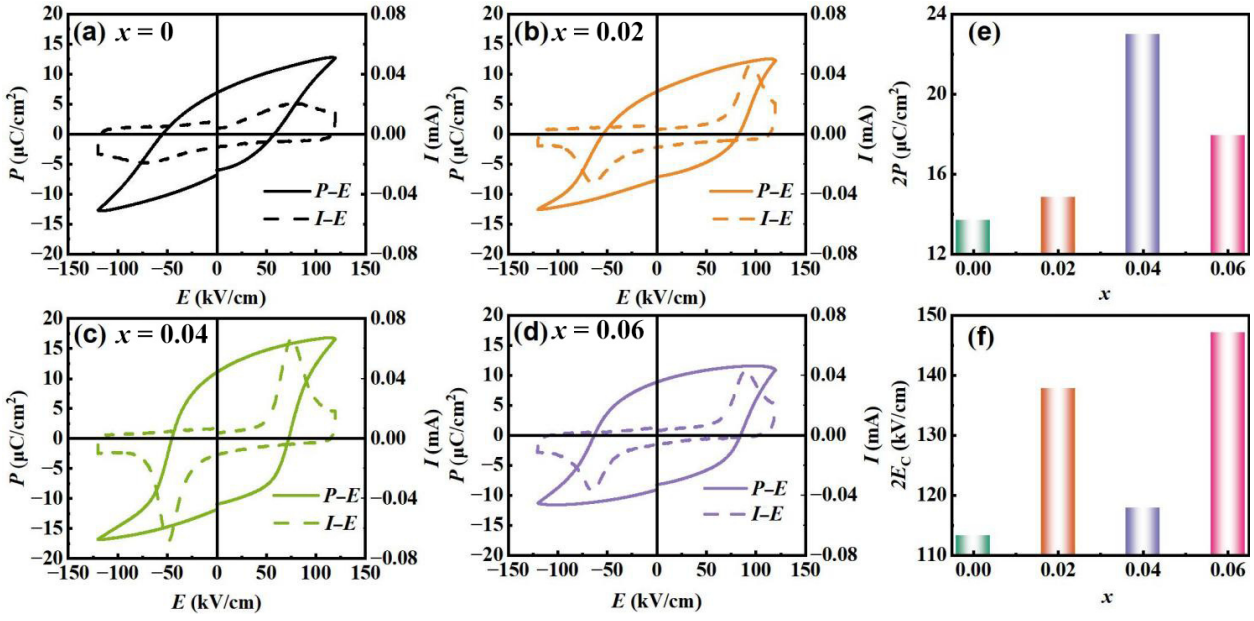

Fig. 9 (a–d) *P*–*E* and *I*–*E* curves of 0.3NBN–0.7BTN–WC_x ceramics at 160 °C and 10 Hz. (e, f) Variation of $2E_C$ and $2P_r$ with *x*.

present the variations in the remnant polarization ($2P_r$) and coercive field ($2E_c$) versus *x*. As the W/Cr co-doping level increases, the $2P_r$ increases from 13.72 μC/cm² (*x* = 0) to 23.02 μC/cm² (*x* = 0.04). The ceramic sample with *x* = 0.04 shows the lowest coercive field of $2E_c$ = 117.91 kV/cm, demonstrating that an optimal amount of W/Cr reduces the concentration of $V_{\ddot{O}}$, thereby weakening the pinning effect of $V_{\ddot{O}}$ on the domains. This reduction in inter-domain coupling lowers the energy barrier for polarization switching and facilitates polarization rotation [49]. Furthermore, according to the piezoelectric equation $d_{33} = 2\varepsilon P_r Q$ [28,50,51], the increase in P_r contributes to enhanced piezoelectric properties of the ceramic.

To explore the influence of domain structure on piezoelectric properties, piezoresponse force microscopy was performed on ceramic samples with optimal compositions at *x* = 0 and *x* = 0.04. This analysis aimed to investigate the local piezoelectric effect and polarization switching behavior. The amplitude images in Figs. 10(a1) and 10(b1), which reflect the piezoelectric response strength, clearly show a stronger piezoelectric response for the *x* = 0.04 sample compared with the *x* = 0 sample. Figures 10(a2) and 10(b2) present the corresponding phase images, which indicate the polarization direction. To further analyze the domain structure, a red line was used to characterize the orientation of the domain walls. Clearly, a higher density of 180° domain walls is observed in the *x* = 0.04 composition. Since 180° domain walls are inherently less stable than other types, they exhibit a stronger response to the electric poling field. As depicted in Figs. 10(c1) and 10(d1), both *x* = 0 and *x* = 0.04 show varying degrees of domain switching under a applied voltage of 30 V within a selected area of 5 μm × 5 μm, with more complete domain switching observed in the *x* = 0.04 composition. This behavior is attributed to the W/Cr components promoting the formation of smaller domains and a higher density of domain walls [38,52]. To assess the sensitivity of the domain response to the applied voltage, relaxation tests were conducted on both compositions with varying relaxation times, and the results are shown in Figs. 10(c3) and 10(d3). The domains in the *x* = 0 sample almost completely disappeared 10 min after the removal of the voltage, whereas those in the *x* = 0.04 composition exhibited remarkable stability. This enhanced stability can be attributed to the high density of domain walls, which induces increased internal stress, thereby hindering domain switching after the electric field is removed and preserving a higher P_r value, as shown in Fig. 9(e). These findings align with the *P*–*E* hysteresis loops shown in Fig. 9, and the stabilized domain configuration further enhances the piezoelectric performance of the ceramic.

To assess the temperature stability of the piezoelectric properties, the 0.3NBN–0.7BTN–WC_x ceramics underwent depolarization treatment, as depicted in Fig. 11(a). All samples exhibited excellent stability. The inset in Fig. 11(a) highlights that the component with *x* = 0.04 exhibits the best room temperature piezoelectric performance, with a d_{33} value of 20.3 pC/N, which is more than 1.8 times that of the component with *x* = 0. At 600 °C, the *x* = 0.04 composition still maintained a relatively high d_{33} value of 18.9 pC/N, retaining 93.1% of its original piezoelectric performance, which indicates the remarkable stability of this ceramic at elevated temperatures. Furthermore, Fig. 11(b) compares the d_{33} and T_C of this work with those of modified BTN-based and NBN-based ceramics reported in the literature [16–18,32,53–63]. The results indicate that this study not only enhances the piezoelectric coefficient of the ceramic but also maintains a high Curie temperature, making it advantageous for high-temperature applications.

4 Conclusions

In summary, a novel solid solution combined with complex ion substitution was developed to design high-temperature BTN-based ceramics with both an enhanced piezoelectric coefficient and resistivity. The results demonstrate that the introduction of W/Cr disrupts the long-range order of the crystal structure, resulting in dielectric relaxation and notable octahedral distortion. Additionally, the reduced oxygen vacancy concentration and lower coercive field decrease the energy barrier for domain switching, thereby facilitating polarization rotation and improving both the resistivity and piezoelectric performance of the ceramics. PFM analysis shows that for the component with *x* = 0.04, the number of 180° domains increases, which leads to more active domain wall motion and a stronger piezoelectric response compared with the sample with *x* = 0. As a result, the W/Cr-doped composition at *x* = 0.04 achieves excellent piezoelectric performance and resistivity, with d_{33} = 20.3 pC/N and ρ = 7.3×

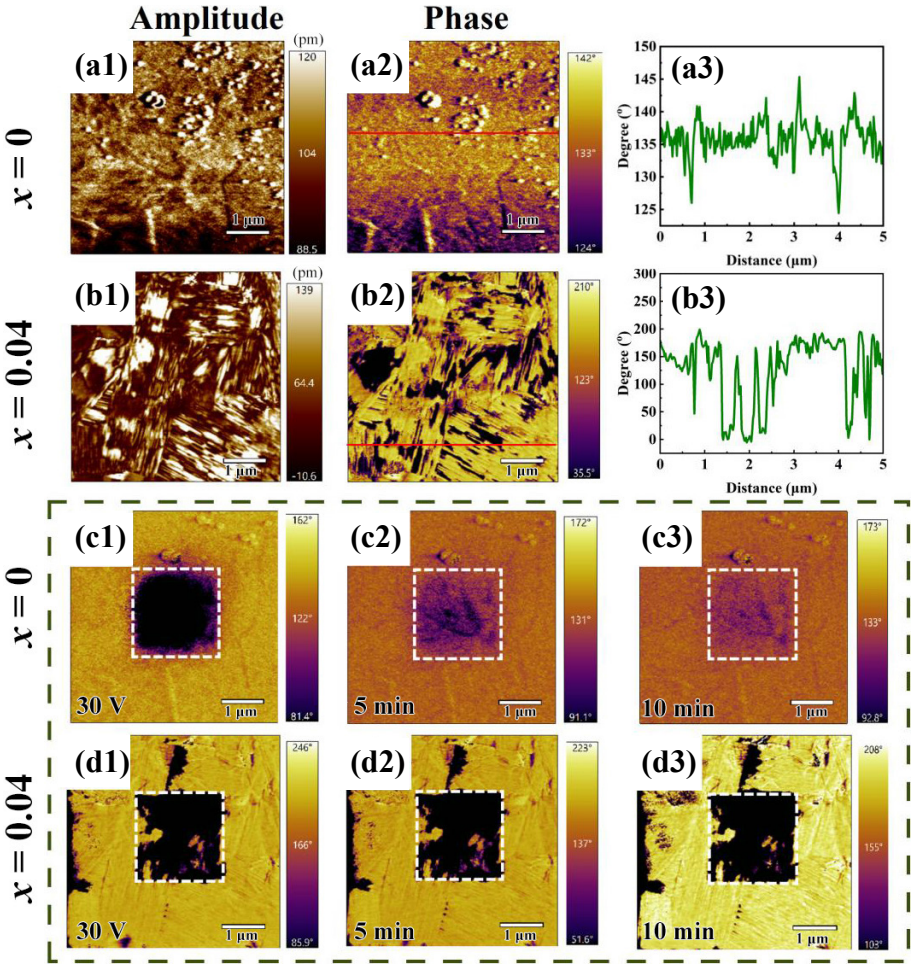

Fig. 10 PFM images of 0.3NBN–0.7BTN–WC_x (x = 0, 0.04) ceramics: (a1, b1) x = 0, 0.04 amplitude. (a2, b2) x = 0, 0.04 phase. (a3, b3) x = 0, 0.04 red line scanning plot of phase diagrams. (c1, d3) Out-of-plane (OOP) PFM phase images of samples with x = 0 and x = 0.04 after removing voltage for 5–10 min.

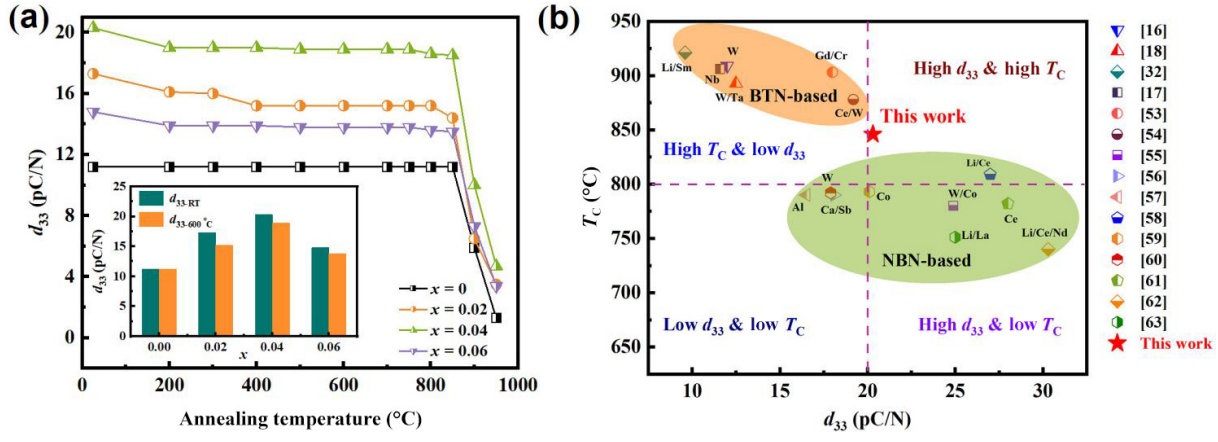

Fig. 11 (a) Thermal depolarization behavior of 0.3NBN–0.7BTN–WC_x ceramics, where inset shows piezoelectric constant d_{33} at room temperature and 600 °C. (b) Correlation between T_C and d_{33} of NBN-based and BTN-based ceramics with different doping elements.

10^7 Ω·cm (@500 °C). This work provides an effective strategy for designing high-performance high-temperature piezoelectrics through simultaneous crystal structure and defect engineering.

Acknowledgements

This work was supported by the Key Research & Development Project of Jiangxi Province (No. 20223BBE51018) and the Graduate Innovation Fund of Jiangxi Province (No. YC2024-B241).

Availability of data and materials

The data that support the findings of this study are available from the corresponding author upon reasonable request.

Competing interests

The authors have no competing interests to declare that are relevant to the content of this article. The author Zong-Yang Shen is the Associate Editor of this journal.

References

[1] Zhang SJ, Yu FP. Piezoelectric materials for high temperature sensors. *J Am Ceram Soc* 2011, **94**: 3153–3170.

[2] Damjanovic D. Materials for high temperature piezoelectric transducers. *Curr Opin Solid St M* 1998, **3**: 469–473.

[3] Turner RC, Fuierer PA, Newnham RE, *et al.* Materials for high temperature acoustic and vibration sensors: A review. *Appl Acoust* 1994, **41**: 299–324.

[4] Nie PC, Li FZ, Ke H, *et al.* Advances in piezoelectric properties of textured ferroelectric ceramics with perovskite structure. *Adv Ceram* 2025, **46**: 171–194. (in Chinese)

[5] Go SH, Park SJ, Kim SH, *et al.* [001]-texturing of $(K,Na)NbO_3$-based piezoceramics with a pseudocubic structure and their application to piezoelectric devices. *J Materiomics* 2024, **10**: 632–642.

[6] Huan Y, Wang XJ, Yang WY, *et al.* Optimizing energy harvesting performance by tailoring ferroelectric/relaxor behavior in KNN-based piezoceramics. *J Adv Ceram* 2022, **11**: 935–944.

[7] Jiang C, Zhou XF, Zhou KC, *et al.* Grain oriented $Na_{0.5}Bi_{0.5}TiO_3$–$BaTiO_3$ ceramics with giant strain response derived from single-crystalline $Na_{0.5}Bi_{0.5}TiO_3$–$BaTiO_3$ templates. *J Eur Ceram Soc* 2016, **36**: 1377–1383.

[8] Zhu CX, Qian J, Tang LM, *et al.* Ultra-high energy harvester performance in KNN-based textured piezoceramics via multiscale reconfiguration design. *J Adv Ceram* 2025, **14**: 9221167.

[9] Wu YJ, Chen J, Yuan J, *et al.* Structure refinements and the influences of A-site vacancies on properties of $Na_{0.5}Bi_{2.5}Nb_2O_9$-based high temperature piezoceramics. *J Appl Phys* 2016, **120**: 194103.

[10] Nayak P, Badapanda T, Singh AK, *et al.* Possible relaxation and conduction mechanism in W^{6+} doped $SrBi_4Ti_4O_{15}$ ceramic. *Ceram Int* 2017, **43**: 4527–4535.

[11] Takenaka T, Nagata H. Current status and prospects of lead-free piezoelectric ceramics. *J Eur Ceram Soc* 2005, **25**: 2693–2700.

[12] Subbarao EC. A family of ferroelectric bismuth compounds. *J Phys Chem Solids* 1962, **23**: 665–676.

[13] Zhou ZY, Dong XL, Yan HX, *et al.* Doping effects on the electrical conductivity of bismuth layered Bi_3TiNbO_9-based ceramics. *J Appl Phys* 2006, **100**: 044112.

[14] Wang Q, Wang CM, Wang JF, *et al.* High performance Aurivillius-type bismuth titanate niobate (Bi_3TiNbO_9) piezoelectric ceramics for high temperature applications. *Ceram Int* 2016, **42**: 6993–7000.

[15] Hou DW, Fan HQ, Yang F, *et al.* Effect of ions substitution with different radii on BO_6 octahedral distortion of Bi_3TiNbO_9 high temperature piezoelectric ceramics. *Mater Lett* 2022, **325**: 132866.

[16] Zhou ZY, Dong XL, Chen H, *et al.* Structural and electrical properties of W^{6+}-doped Bi_3TiNbO_9 high-temperature piezoceramics. *J Am Ceram Soc* 2006, **89**: 1756–1760.

[17] Zhang YH, Huang PM, Zhu LL, *et al.* Doping level effects in Nb self-doped Bi_3TiNbO_9 high-temperature piezoceramics with improved electrical properties. *Int J Appl Ceram Tec* 2020, **17**: 2407–2415.

[18] Peng ZH, Yan DX, Chen Q, *et al.* Crystal structure, dielectric and piezoelectric properties of Ta/W codoped Bi_3TiNbO_9 Aurivillius phase ceramics. *Curr Appl Phys* 2014, **14**: 1861–1866.

[19] Wu HS, Shen ZY, Wen QL, *et al.* Significantly enhanced piezoelectric response in Aurivillius Bi_3TiNbO_9 ceramics simply by Ce doping. *Ceram Int* 2024, **50**: 50177–50184.

[20] Tian X, Qu SB, Wang B, *et al.* Microstructure and electrical properties of ultra high temperature $(1–x)CaBi_2Nb_2O_9$–$xNa_{0.5}Bi_{2.5}Nb_2O_9$ ceramics. *Mater Res Innov* 2015, **19**: 171–175.

[21] Zhang ZP, Li YX, Shen ZY, *et al.* Structural evolution and electrical properties of a new $xNa_{0.5}Bi_{2.5}Nb_2O_9$–$(1–x)Bi_3TiNbO_9$ solid solution for high-temperature piezoelectric ceramics. *J Alloy Compd* 2025, **1042**: 184164.

[22] Hou JG, Qu YF, Vaish R, *et al.* Crystallographic evolution, dielectric, and piezoelectric properties of $Bi_4Ti_3O_{12}$:W/Cr ceramics. *J Am Ceram Soc* 2010, **93**: 1414–1421.

[23] Xu BJ, Jiang XP, Zeng RF, *et al.* Deciphering the structural and electrical properties of Ce and Ta ion-doped $Bi_3Ti_{1.5}W_{0.5}O_9$ bismuth layered piezoelectric ceramics. *Mat Sci Semicon Proc* 2025, **192**: 109442.

[24] Zhou ZY, Cheng BZ, Li YC, *et al.* Preparation of textured Bi_3TiNbO_9 ceramics. *Mater Chem Phys* 2007, **104**: 225–229.

[25] Guan SY, Wu XJ, Shi W, *et al.* Enhanced piezoelectric response of Aurivillius ferroelectrics by constructing a novel solid solution and combining traditional chemical substitution. *J Appl Phys* 2023, **133**: 014103.

[26] Wu DW, Zhou HJ, Li LF, *et al.* Gd/Mn co-doped $CaBi_4Ti_4O_{15}$ Aurivillius-phase ceramics: Structures, electrical conduction and dielectric relaxation behaviors. *Materials* 2022, **15**: 5810.

[27] Wen QL, Guo HH, Shen ZY, *et al.* MnO_2 doping induced structural tuning drives superior piezoelectric response in $CaBi_4Ti_4O_{15}$-based ceramics. *J Adv Ceram* 2025, **14**: 9221051.

[28] Xu BJ, Jiang XP, Zeng RF, *et al.* Strategies to enhance the piezoelectric properties of $Bi_3Ti_{1.5}W_{0.5}O_9$ ceramics and analyze the conductive mechanism based on subtle lattice contribution and domain response. *J Alloy Compd* 2025, **1018**: 179224.

[29] Osada M, Tada M, Kakihana M, *et al.* Cation distribution and structural instability in $Bi_{4-x}La_xTi_3O_{12}$. *Jpn J Appl Phys* 2001, **40**: 5572.

[30] Yuan J, Nie R, Chen Q, *et al.* Structural distortion, piezoelectric properties, and electric resistivity of A-site substituted Bi_3TiNbO_9-based high-temperature piezoceramics. *Mater Res Bull* 2019, **115**: 70–79.

[31] Zhu JS, Qin HX, Bao ZH, *et al.* X-ray diffraction and Raman scattering study of $SrBi_2Ta_2O_9$ ceramics and thin films with Bi_3TiNbO_9 addition. *Appl Phys Lett* 2001, **79**: 3827–3829.

[32] Hou DW, Fan HQ, Zhang A, *et al.* Role of BO_6 octahedral distortion on high temperature piezoelectric properties in $Bi_{3-x}(Li_{0.5}Sm_{0.5})_xTiNbO_9$. *Ceram Int* 2022, **48**: 22163–22171.

[33] Dobal PS, Katiyar RS. Studies on ferroelectric perovskites and bi-layered compounds using micro-Raman spectroscopy. *J Raman Spectrosc* 2002, **33**: 405–423.

[34] Wu XJ, Shi W, Guan SY, *et al.* Realization of high electric performance in Aurivillius ferroelectrics via combining chemical substitution and the construction of new-type solid solution systems. *J Eur Ceram Soc* 2022, **42**: 119–128.

[35] Chen Y, Xie SX, Wang QY, *et al.* Influence of Cr_2O_3 additive and sintering temperature on the structural characteristics and piezoelectric properties of $Bi_4Ti_{2.95}W_{0.05}O_{12.05}$ Aurivillius ceramics. *Prog Nat Sci—Mater* 2016, **26**: 572–578.

[36] Shen ZY, Zhang ZP, Qin C, *et al.* Effect of $(K_{0.5}Ce_{0.5})$ complex on the electrical properties of lead-free $Bi_4Ti_{2.86}W_{0.14}O_{12}$ high-temperature piezoelectric ceramics. *J Mater Res* 2021, **36**: 1134–1141.

[37] Peng ZH, Chen Q, Chen Y, *et al.* Microstructure and electrical properties in W/Nb co-doped Aurivillius phase $Bi_4Ti_3O_{12}$ piezoelectric ceramics. *Mater Res Bull* 2014, **59**: 125–130.

[38] Xie SX, Xu Q, Chen Q, *et al.* Realizing super-high piezoelectricity and excellent fatigue resistance in domain-engineered bismuth titanate ferroelectrics. *Adv Funct Mater* 2024, **34**: 2312645.

[39] He Q, Nie JK, Han Y, *et al.* Effect of Ge^{4+} doping on sintering and electrical properties of potassium sodium niobate-based lead-free piezoelectric ceramics. *J Ceram* 2022, **43**: 1023–1029. (in Chinese)

[40] Wang CL, Hou LM, Huan Y. Study on the structure and properties of $(1–x)$KNNS–xBFANZ lead-free piezoelectric ceramics. *Adv Ceram* 2023, **44**: 490–496. (in Chinese)

[41] Chen XY, Ou B, Liu GF, *et al.* Simultaneous enhancement of piezoelectric performance and Curie temperature in high-temperature $Bi_4Ti_3O_{12}$ piezoceramics through A/B site co-doping. *J Adv Ceram* 2025, **14**: 9221077.

[42] Yang AH, Huan Y, Wang QY, *et al.* Excellent comprehensive piezoelectric performances of SiC-doped BCTZ-based lead-free piezoelectric ceramics. *J Adv Ceram* 2025, **14**: 9221054.

[43] Luo XG, Yan ZN, Luo H, *et al.* Greatly improved piezoelectricity and thermal stability of (Na, Sm) co-doped $CaBi_2Nb_2O_9$ ceramics. *Adv Powder Mater* 2023, **2**: 100116.

[44] Shulman HS, Testorf M, Damjanovic D, *et al.* Microstructure,

electrical conductivity, and piezoelectric properties of bismuth titanate. *J Am Ceram Soc* 1996, **79**: 3124–3128.
[45] Chen Y, Zhou HJ, Wang SZ, *et al.* Diffused phase transition, ionic conduction mechanisms and electric-field dependent ferroelectricity of Nb/Ce co-doped $Pb(Zr_{0.52}Ti_{0.48})O_3$ ceramics. *J Alloy Compd* 2021, **854**: 155500.
[46] Guan SY, Wang B, Shi W, *et al.* Realization of high piezoelectric performance in bismuth titanate niobate via B-site mixed-valance doping. *J Eur Ceram Soc* 2023, **43**: 928–938.
[47] Pan Y, Zhang Y, Dong QP, *et al.* Entropy-driven multi-scale enhancement of energy storage performance in $(Bi_{0.5}Na_{0.5})_{0.5}Ba_{0.5}TiO_3$ ceramics. *J Materiomics* 2025, **11**: 101055.
[48] Hu ZM, Koval V, Zhang HF, *et al.* Enhanced piezoelectricity in Na and Ce co-doped $CaBi_4Ti_4O_{15}$ ceramics for high-temperature applications. *J Adv Ceram* 2023, **12**: 1331–1344.
[49] Wu J, Ma XS, Zhou DH, *et al.* High-entropy high-temperature high-piezoelectricity ceramics. *Adv Mater* 2025, **37**: 2419134.
[50] Park SE, Shrout TR. Characteristics of relaxor-based piezoelectric single crystals for ultrasonic transducers. *IEEE T Ultrason Ferr* 1997, **44**: 1140–1147.
[51] Wang XP, Wu JG, Xiao DQ, *et al.* Large d_{33} in $(K,Na)(Nb,Ta,Sb)O_3$–$(Bi,Na,K)ZrO_3$ lead-free ceramics. *J Mater Chem A* 2014, **2**: 4122–4126.
[52] Yang ZT, Gao F, Du HL, *et al.* Grain size engineered lead-free ceramics with both large energy storage density and ultrahigh mechanical properties. *Nano Energy* 2019, **58**: 768–777.
[53] Chen Y, Zhou HJ, Wang QY, *et al.* Doping level effects in Gd/Cr co-doped Bi_3TiNbO_9 Aurivillius-type ceramics with improved electrical properties. *J Materiomics* 2022, **8**: 906–917.
[54] Yuan J, Nie R, Chen Q, *et al.* Evolution of structural distortion and electric properties of BTN-based high-temperature piezoelectric ceramics with tungsten substitution. *J Alloy Compd* 2019, **785**: 475–483.
[55] Jie ST, Jiang XP, Chen C, *et al.* Influence of Co/W co-doping on structural and electrical properties of $Na_{0.5}Bi_{2.5}Nb_2O_9$ piezoelectric ceramics. *Ceram Int* 2022, **48**: 6258–6265.
[56] Chen Q, Peng ZH, Liu H, *et al.* Effects of (Ca,Sb) on the properties of $Na_{0.5}Bi_{2.5}Nb_2O_9$-based bismuth layered structure ferroelectric ceramics. *Ferroelectrics* 2013, **455**: 169–175.
[57] Zhou ZY, Liang RH, Li YC, *et al.* Enhanced electrical resistivity of Al_2O_3 addition modified $Na_{0.5}Bi_{2.5}Nb_2O_9$ high-temperature piezoceramics. *J Am Ceram Soc* 2015, **98**: 3925–3929.
[58] Gai ZG, Wang JF, Zhao ML, *et al.* High temperature $(NaBi)_{0.48}\square_{0.04}Bi_2Nb_2O_9$-based piezoelectric ceramics. *Appl Phys Lett* 2006, **89**: 012907.
[59] Jie ST, Jiang XP, Chen C, *et al.* Effect of Co^{3+} on structure and electrical properties of $Na_{0.5}Bi_{2.5}Nb_2O_9$ ceramics. *J Mater Sci—Mater El* 2021, **32**: 23834–23842.
[60] Zhou ZY, Li YC, Hui SP, *et al.* Effect of tungsten doping in bismuth-layered $Na_{0.5}Bi_{2.5}Nb_2O_9$ high temperature piezoceramics. *Appl Phys Lett* 2014, **104**: 012904.
[61] Wang XJ, Jiang XP, Chen CR, *et al.* Effect of Ce-doping on properties of $0.9Na_{0.5}Bi_{2.5}Nb_2O_9$–$0.1LiNbO_3$-based high temperature lead-free piezoelectric ceramics. *J Synth Cryst* 2012, **41**: 1254–1259.
[62] Wang J, Fan WY, Cheng SD, *et al.* Multiscale structural engineering boosts piezoelectricity in $Na_{0.5}Bi_{2.5}Nb_2O_9$-based high-temperature piezoceramics. *ACS Appl Mater Inter* 2024, **16**: 19150–19157.
[63] Long CB, Fan HQ, Li MM. High temperature Aurivillius piezoelectrics: The effect of (Li, Ln) modification on the structure and properties of $(Li,Ln)_{0.06}(Na,Bi)_{0.44}Bi_2Nb_2O_9$ (Ln = Ce, Nd, La and Y). *Dalton T* 2013, **42**: 3561–3570.